This document is the accepted manuscript version of the following article: Buizert, C., Sigl, M., Severi, M., Markle, B. R., Wettstein, J. J., McConnell, J. R., ... Steig, E. J. (2018). Abrupt ice-age shifts in southern westerly winds and Antarctic climate forced from the north. Nature, 563(7733), 681-685. https://doi.org/10.1038/s41586-018-0727-5

#### 1 Abrupt Ice Age Shifts in Southern Westerlies and Antarctic Climate Forced from

## 2 the North

Christo Buizert<sup>1</sup>, Michael Sigl<sup>2</sup>, Mirko Severi<sup>3</sup>, Bradley R. Markle<sup>4</sup>, Justin J. Wettstein<sup>1,5</sup>,
Joseph R. McConnell<sup>6</sup>, Joel B. Pedro<sup>7,8</sup>, Harald Sodemann<sup>5</sup>, Kumiko Goto-Azuma<sup>9</sup>, Kenji Kawamura<sup>9</sup>,
Shuji Fujita<sup>9</sup>, Hideaki Motoyama<sup>9</sup>, Motohiro Hirabayashi<sup>9</sup>, Ryu Uemura<sup>10</sup>, Barbara Stenni<sup>11</sup>,
Frédéric Parrenin<sup>12</sup>, Feng He<sup>1,13</sup>, T.J. Fudge<sup>4</sup> and Eric J. Steig<sup>4</sup>

- 7 <sup>1</sup>College of Earth, Ocean and Atmospheric Sciences, Oregon State University, Corvallis OR 97331, USA
- 8 <sup>2</sup>Laboratory of Environmental Chemistry, Paul Scherrer Institute, Villigen, Switzerland
- 9 <sup>3</sup>Department of Chemistry "Ugo Schiff", University of Florence, Florence, Italy
- <sup>4</sup>Department of Earth and Space Science, University of Washington, Seattle WA 98195, USA
- <sup>5</sup>Geophysical Institute and Bjerknes Centre for Climate Research, University of Bergen, 5020 Bergen,
- 12 Norway
- <sup>6</sup>Desert Research Institute, Nevada System of Higher Education, Reno, NV 89512, USA
- <sup>14</sup> <sup>7</sup>Centre for Ice and Climate, Niels Bohr Institute, University of Copenhagen, Copenhagen, Denmark
- <sup>8</sup>Antarctic Climate & Ecosystems Cooperative Research Centre, University of Tasmania, Private Bag 80,
- 16 Hobart, Tasmania 7001, Australia
- <sup>9</sup>National Institute for Polar Research, Tachikawa, Tokyo, Japan
- <sup>10</sup>Department of Chemistry, Biology and Marine Science, University of the Ryukyus, Okinawa, Japan
- <sup>11</sup>Department of Environmental Sciences, Informatics and Statistics, Ca' Foscari University of Venice,
- 20 30172 Venezia, Italy
- 21 <sup>12</sup>Université Grenoble Alpes, CNRS, IRD, IGE, 38000 Grenoble, France
- <sup>13</sup>Center for Climatic Research, Nelson Institute for Environmental Studies, University of Wisconsin-
- 23 Madison, Madison WI 53706, USA

The Southern Hemisphere (SH) mid-latitude westerly winds play a central role in the global 24 climate system via Southern Ocean upwelling<sup>1</sup>, carbon exchange with the deep ocean<sup>2</sup>, 25 Agulhas Leakage<sup>3</sup>, and possibly Antarctic ice sheet stability<sup>4</sup>. Meridional shifts of the SH 26 westerlies have been hypothesized in response to abrupt North Atlantic Dansgaard-Oeschger 27 (DO) climatic events of the last ice age<sup>5,6</sup>, in parallel with the well-documented shifts of the 28 intertropical convergence zone (ITCZ)<sup>7</sup>. Shifting moisture pathways to West Antarctica<sup>8</sup> are 29 consistent with this view, but may represent a Pacific teleconnection pattern<sup>9</sup>. The full SH 30 31 atmospheric-circulation response to the DO cycle and its impact on Antarctic temperature remain unclear<sup>10</sup>. Here we use five volcanically-synchronized ice cores to show that the 32 Antarctic temperature response to the DO cycle can be understood as the superposition of 33 two modes: a spatially homogeneous oceanic "bipolar seesaw" mode that lags Northern 34 Hemisphere (NH) climate by about 200 years, and a spatially heterogeneous atmospheric 35 36 mode that is synchronous with NH abrupt events. Temperature anomalies of the atmospheric mode are similar to those associated with present-day Southern Annular Mode (SAM) 37 variability, rather than the Pacific South America (PSA) pattern. Moreover, deuterium excess 38 records suggest a zonally coherent migration of the SH westerlies over all ocean basins in 39 phase with NH climate. Our work provides a simple conceptual framework for understanding 40 41 the circum-Antarctic temperature response to abrupt NH climate change. We provide observational evidence for abrupt shifts in the SH westerlies, which has previously-42 documented<sup>1-3</sup> ramifications for global ocean circulation and atmospheric CO<sub>2</sub>. These coupled 43 changes highlight the necessity of a global, rather than a purely North Atlantic, perspective on 44 the DO cycle. 45

During the glacial DO cycle, abrupt variations in northward heat transport by the Atlantic 46 47 Meridional Overturning Circulation (AMOC) affect Greenland and Antarctic temperature oppositely (Fig. 1), via an oceanic teleconnection called the bipolar seesaw<sup>6,11</sup>. Antarctica warms 48 during Greenland cold phases (stadials), and cools during Greenland warmth (interstadials), 49 with the gradual nature of Antarctic climate change reflecting buffering by a large heat 50 reservoir<sup>11</sup> – likely the global ocean interior<sup>6</sup>. The DO cycle affects atmospheric circulation also; 51 the ITCZ shifts southwards during stadials, and northwards during interstadials<sup>7</sup>. General 52 Circulation Model (GCM) simulations suggest parallel shifts of the SH westerlies<sup>5,6,12</sup>, but the 53 available observational evidence (a deuterium excess record from West Antarctica<sup>8</sup>) cannot 54 distinguish between such shifts and Pacific-only teleconnections<sup>9</sup>. Furthermore, the impact of 55 the atmospheric circulation changes on Antarctic climate remains unknown, and models are 56 inconclusive on this question<sup>10,13</sup>. 57

We use water stable isotope ratios, a proxy for site temperature<sup>14</sup>, from five Antarctic ice cores: 58 WAIS (West Antarctic Ice Sheet) Divide (WDC), EPICA (European Project for Ice Coring in 59 Antarctica) Dronning Maud Land (EDML), EPICA Dome C (EDC), Dome Fuji (DF) and Talos Dome 60 (TAL). WDC is synchronized to Greenland ice cores at high precision via atmospheric methane 61 (Fig. 1a, b)<sup>15</sup>; here we synchronize WDC to the other cores in the 10-57 ka before present (BP) 62 interval using volcanic markers (Methods; Extended Data Figure 1), greatly improving our ability 63 64 to study the timing of regional Antarctic climate variations relative to Greenland. The Antarctic response to DO events is investigated using a stacking technique, in which 19 individual events 65 are aligned at the midpoint of their abrupt methane transition in the WDC core, and averaged 66 67 to obtain the shared climatic signal (Methods).

Antarctica cools in response to DO warming (Fig. 2a, b), consistent with the bipolar seesaw theory<sup>6,11</sup>. In the Antarctic mean  $\delta^{18}$ O stack, the cooling onset occurs about two centuries after the abrupt NH event, providing validation of earlier results from West Antarctica<sup>15</sup>. There is a spatial pattern to the Antarctic response, however. A step-like divergence from the mean signal is seen around  $t \approx 0$  yr (i.e., synchronous with NH climate), with the interior East Antarctic Plateau sites (DF and EDC) warming, and EDML cooling (Fig. 2c). This instantaneous warming over the Plateau is particularly pronounced at DO events 1, 8, 12 and 14 (Fig. 1d, red curve).

Using principal component analysis (PCA, see Methods), we find that two modes of variability explain over 96% of signal variance in the five stacked records (Fig. 2d). The first principal component (PC1, 83% of variance explained) has the triangular shape of the Antarctic Isotope Maximum events – the classic thermal bipolar seesaw signal<sup>11</sup> – with a spatially homogeneous expression (Fig. 2f). The two-century lag behind Greenland warming identifies PC1 as an oceanpropagated response<sup>15</sup>.

81 The second principal component (PC2, 13% of variance explained) is a step-like function with a 82 heterogeneous spatial pattern (Fig. 2g). This mode is very different from the bipolar seesaw. 83 The PC2 response is synchronous with NH warming within precision ( $28 \pm 40$  year lag); this timing, and additional evidence presented below, suggest this mode represents an atmospheric 84 85 teleconnection. The PCA does not necessarily separate physical processes. We assume two 86 underlying teleconnections: oceanic (two-century lag) and atmospheric (synchronous). Some amount of each process is included in PC1, as evident by some immediate warming around t=0. 87 We perform a rotation of the PCA vectors (Methods) to isolate the "purely" oceanic and 88 atmospheric responses (Fig. 2e). The associated estimate of the atmospherically-forced 89

temperature anomaly (Fig. 2h) is cooling at EDML, warming at DF, EDC and TAL, and a negligible response at WDC; this pattern is robustly reproduced using different methods (Extended Data Fig. 6). The magnitude of the Antarctic atmospheric response is roughly proportional to the Greenland ice core  $\delta^{18}$ O perturbation (Extended Data Fig. 4).

The Antarctic response to DO cooling is qualitatively similar to the DO warming case. The ocean seesaw warming response is delayed by 226 ± 44 years and the EOF2 spatial pattern has the opposite sign – i.e. additional warming at EDML, and cooling on the interior East Antarctic Plateau (Extended Data Fig. 7). The atmospheric signal over Antarctica is much weaker for the DO cooling case, with PC2 explaining only 9% of variance. This difference is likely due to the fact that DO warmings are more abrupt and of larger magnitude than DO coolings.

To better understand the atmospheric mode, we turn to deuterium excess (d), a proxy for 100 vapor source conditions<sup>16</sup> commonly used to identify changes in atmospheric circulation and 101 vapor transport pathways<sup>8,17,18</sup>. In isotope-enabled GCM simulations, Antarctic d is anti-102 correlated with the Southern Annular Mode (SAM) index<sup>8,19</sup>. This anti-correlation can be 103 104 understood conceptually: when the SH westerlies are displaced equatorward (negative SAM 105 phase), Antarctic moisture will originate further north where sea-surface temperature (SST) is higher and relative humidity lower (Extended Data Fig. 8b), both of which act to make d more 106 positive<sup>16</sup>. We use the logarithmic definition of deuterium excess ( $d_{ln}$ ), which better preserves 107 isotopic moisture source information than the linear definition<sup>8,20</sup>. 108

109 The Antarctic mean  $d_{ln}$  response (Figs. 3a, b) lags NH climate by 8 ± 48 years for DO warming, 110 and 9 ± 42 years for DO cooling, respectively, consistent with previous results for WDC<sup>8</sup>. The

observed  $d_{ln}$  response is consistent with a shift in the meridional position of the SH westerly 111 112 winds and vapor origin, such that they move equatorward in response to NH warming, and poleward in response to NH cooling. The timing suggests propagation to the SH high-latitudes 113 via an atmospheric teleconnection. The  $d_{ln}$  response is largest for the interior Plateau sites (DF, 114 115 EDC), possibly because their vapor source areas are more distant from confounding local effects such as the sea-ice edge<sup>21</sup>. The response is weak or absent at EDML; possibly because SH 116 westerlies' variability is relatively weak in the Atlantic sector (Extended Data Fig. 9), or because 117 118 of regional effects such as wind-driven changes to the sea ice, gyre circulation or Weddell Sea deep convection<sup>22</sup>. Critically, the four cores that do show a clear  $d_{\rm in}$  response collectively 119 sample water vapor from all ocean basins (Extended Data Fig. 8a), suggesting the changes to 120 121 the SH atmospheric circulation are zonally coherent and involve all ocean basins (rather than just the Pacific basin as demonstrated previously with WDC). 122

123 Figure 4a compares the two independent signals we attribute to a change in atmospheric circulation: PC2 of the  $\delta^{18}$ O response, and the Antarctic mean  $d_{ln}$  response. Their time evolution 124 125 is nearly identical, suggesting they are distinct but consistent manifestations of the atmospheric circulation change. The SAM and Pacific-South American (PSA) pattern are the leading modes of 126 large-scale SH atmospheric variability with strong influence on Antarctic temperature<sup>9,23</sup>. We 127 focus our analysis on East Antarctica, where we infer the largest response. The SAM (Fig. 4b) 128 129 clearly impacts East Antarctic surface air temperature (SAT) strongly (correlation |r| up to 130 0.65), and with the correct sign to explain the warming seen at EDC, DF and TAL. East Antarctic warming is seen for a more negative SAM index, driven primarily by anomalous atmospheric 131 heat advection<sup>24</sup> (the observed cooling at EDML is discussed below). The PSA (Fig. 4c), on the 132

other hand, is not meaningfully correlated with SAT at the East Antarctic sites (|*r*| at or below 0.15). We further create a synthetic index that is the projection of the atmospheric loadings (Fig. 2h) onto the reanalysis SAT anomaly at the core locations (Methods). The patterns in SAT and geopotential height associated with this index (Fig. 4d) closely resemble those of the SAM, with warming in East Antarctica, and roughly annular geopotential height anomalies.

These tests suggest that the SAM is the closest present-day analog to the temperature response we identify in the ice core record, corroborating our independent evidence from the  $d_{ln}$  data. While the PSA pattern may have been active during the DO cycle, it does not dominate the Antarctic response.

Our data-based inferences on the timing and sign of changes to the SH westerlies/SAM are 142 consistent with coupled atmosphere-ocean GCM simulations in which AMOC transitions are 143 induced by North Atlantic fresh-water forcing<sup>6,12,25</sup>. Such model simulations show a positive 144 shift in SAM index in response to AMOC shutdown and vice versa (Fig. 3a, b); this shift is 145 synchronous with the applied forcing within uncertainty (Extended Data Table 1). Our observed 146 atmospheric response is more gradual than the model-simulated SAM shift, possibly because of 147 (multi-decadal) data resolution in some cores and the fact that the  $d_{ln}$  signal integrates over a 148 large moisture source area extending to  $20^{\circ}$ S. 149

Next, we address differences between the ice-core data and the modern-day correlation pattern (Fig. 4b), most notably at EDML. The reanalysis correlation pattern captures the SAT response to monthly internal SAM variability, representing atmospheric heat advection anomalies<sup>24</sup>. The ice cores, on the other hand, record the response to a persistent long-term shift in SAM<sup>13,26</sup>, driving changes in SST, stratification and sea ice extent<sup>22,26</sup>. We speculate that
on longer timescales the oceanic influence of the Weddell Sea drives the cooling at EDML, due
to e.g. enhanced sea ice cover<sup>22</sup> and stratification, and a weakening of the wind-driven Weddell
Gyre. The negligible warming response at WDC is consistent with the relatively weak influence
of the SAM in West Antarctic seen in monthly reanalysis (Fig. 4b). Our observations may help
constrain the long-term response to a persistent SAM shift, on which GCMs disagree<sup>13</sup>.

Last, we want to highlight additional structure in the Antarctic  $\delta^{18}$ O stacks that is currently not part of scientific discourse on interhemispheric climate coupling. Most notably, Antarctic warming appears to slow down around *t*=-400 yr (Fig. 2b), forming a secondary change point that precedes the abrupt DO warming events<sup>27</sup>. Likewise, the rate of Antarctic cooling appears to increase 200 years prior to the abrupt DO cooling events (Extended Data Fig. 7b). These secondary change points are subtler than the ones analyzed in this work, have no apparent corresponding features in Antarctic *d*<sub>in</sub> or Greenland climate, and remain unexplained.

In conclusion, our results show that Antarctica is influenced by NH abrupt climate change on two distinct time scales, representing a slow oceanic and a fast atmospheric teleconnection. In particular, we provide observational evidence for zonally-coherent meridional shifts in the SH westerly winds in phase with Greenland DO events, and its impact on Antarctic temperature. Such shifts have implications for global ocean circulation, Southern Ocean upwelling and productivity, and atmospheric  $CO_2^{1-3}$ . It is therefore paramount to consider the DO cycle from a global, rather than a purely North Atlantic perspective.

174

## 175 **References:**

- Marshall, J. & Speer, K. Closure of the meridional overturning circulation through Southern
   Ocean upwelling. *Nature Geosci* 5, 171-180 (2012).
- Toggweiler, J. R., Russell, J. L. & Carson, S. R. Midlatitude westerlies, atmospheric CO<sub>2</sub>, and
   climate change during the ice ages. *Paleoceanography* **21**, PA2005, doi:10.1029/2005pa001154
   (2006).
- Biastoch, A., Boning, C. W., Schwarzkopf, F. U. & Lutjeharms, J. R. E. Increase in Agulhas leakage
  due to poleward shift of Southern Hemisphere westerlies. *Nature* 462, 495-U188,
  doi:10.1038/nature08519 (2009).
- Pritchard, H. D. *et al.* Antarctic ice-sheet loss driven by basal melting of ice shelves. *Nature* 484, 502-505, doi:10.1038/nature10968 (2012).
- Lee, S. Y., Chiang, J. C., Matsumoto, K. & Tokos, K. S. Southern Ocean wind response to North
   Atlantic cooling and the rise in atmospheric CO<sub>2</sub>: Modeling perspective and paleoceanographic
   implications. *Paleoceanography* **26** (2011).
- Pedro, J. B. *et al.* Beyond the bipolar seesaw: Toward a process understanding of
  interhemispheric coupling. *Quat. Sci. Rev.* **192**, 27-46, doi:10.1016/j.quascirev.2018.05.005
  (2018).
- 1927Schneider, T., Bischoff, T. & Haug, G. H. Migrations and dynamics of the intertropical193convergence zone. Nature **513**, 45-53 (2014).
- Markle, B. R. *et al.* Global atmospheric teleconnections during Dansgaard-Oeschger events.
   *Nature Geosci* 10, 36-40, doi:10.1038/ngeo2848 (2017).
- 1969Ding, Q., Steig, E. J., Battisti, D. S. & Kuttel, M. Winter warming in West Antarctica caused by197central tropical Pacific warming. Nature Geosci 4, 398-403, doi:10.1038/ngeo1129 (2011).
- 19810Buiron, D. *et al.* Regional imprints of millennial variability during the MIS 3 period around199Antarctica. *Quat. Sci. Rev.* 48, 99-112, doi:10.1016/j.quascirev.2012.05.023 (2012).
- Stocker, T. F. & Johnsen, S. J. A minimum thermodynamic model for the bipolar seesaw.
   *Paleoceanography* 18, 1087, doi:10.1029/2003pa000920 (2003).
- 202 12 Rind, D. *et al.* Effects of glacial meltwater in the GISS coupled atmosphere-ocean model: 2. A
  203 bipolar seesaw in Atlantic Deep Water production. *Journal of Geophysical Research:*204 *Atmospheres (1984–2012)* 106, 27355-27365 (2001).
- 20513Kostov, Y. *et al.* Fast and slow responses of Southern Ocean sea surface temperature to SAM in206coupled climate models. *Clim. Dyn.* **48**, 1595-1609, doi:10.1007/s00382-016-3162-z (2017).
- Jouzel, J. *et al.* Validity of the temperature reconstruction from water isotopes in ice cores. *J. Geophys. Res.* **102**, 26471-26487, doi:10.1029/97jc01283 (1997).
- 20915WAIS-Divide-Project-Members. Precise interpolar phasing of abrupt climate change during the210last ice age. Nature **520**, 661-665, doi:10.1038/nature14401 (2015).
- 21116Merlivat, L. & Jouzel, J. Global climatic interpretation of the deuterium-oxygen 18 relationship212for precipitation. J. Geophys. Res. 84, 5029-5033, doi:10.1029/JC084iC08p05029 (1979).
- 21317Masson-Delmotte, V. *et al.* GRIP Deuterium Excess Reveals Rapid and Orbital-Scale Changes in214Greenland Moisture Origin. *Science* **309**, 118-121 (2005).
- 21518Masson-Delmotte, V. *et al.* Abrupt change of Antarctic moisture origin at the end of Termination216II. *Proc. Natl. Acad. Sci. U. S. A.* **107**, 12091-12094, doi:10.1073/pnas.0914536107 (2010).
- Schmidt, G. A., LeGrande, A. N. & Hoffmann, G. Water isotope expressions of intrinsic and
  forced variability in a coupled ocean-atmosphere model. *J. Geophys. Res.* **112** (2007).
- 20 Uemura, R. *et al.* Ranges of moisture-source temperature estimated from Antarctic ice cores
  stable isotope records over glacial-interglacial cycles. *Clim. Past* 8, 1109-1125, doi:10.5194/cp-81109-2012 (2012).

222	21	Sodemann, H. & Stohl, A. Asymmetries in the moisture origin of Antarctic precipitation.	
223		Geophys. Res. Lett. <b>36</b> , L22803, doi:10.1029/2009gl040242 (2009).	
224	22	Lefebvre, W., Goosse, H., Timmermann, R. & Fichefet, T. Influence of the Southern Annular	
225		Mode on the sea ice-ocean system. J. Geophys. Res. 109, C09005, doi:10.1029/2004JC002403	
226		(2004).	
227	23	Thompson, D. W. J. & Wallace, J. M. Annular Modes in the Extratropical Circulation. Part I:	
	25	• • • •	
228		Month-to-Month Variability*. J. Clim. <b>13</b> , 1000-1016, doi:10.1175/1520-	
229		0442(2000)013<1000:amitec>2.0.co;2 (2000).	
230	24	Sen Gupta, A. & England, M. H. Coupled ocean-atmosphere-ice response to variations in the	
231		Southern Annular Mode. <i>J. Clim.</i> <b>19</b> , 4457-4486 (2006).	
232	25	Liu, Z. et al. Transient Simulation of Last Deglaciation with a New Mechanism for Bolling-Allerod	
233		Warming. Science <b>325</b> , 310-314, doi:10.1126/science.1171041 (2009).	
234	26	Ferreira, D., Marshall, J., Bitz, C. M., Solomon, S. & Plumb, A. Antarctic Ocean and Sea Ice	
235		Response to Ozone Depletion: A Two-Time-Scale Problem. J. Clim. 28, 1206-1226,	
236		doi:10.1175/JCLI-D-14-00313.1 (2014).	
	27		
237	27	Raisbeck, G. M. <i>et al.</i> An improved north–south synchronization of ice core records around the	
238		41 kyr 10Be peak. <i>Clim. Past</i> <b>13</b> , 217-229, doi:10.5194/cp-13-217-2017 (2017).	
239	28	Grootes, P. M., Stuiver, M., White, J. W. C., Johnsen, S. & Jouzel, J. Comparison of oxygen	
240		isotope records from the GISP2 and GRIP Greenland ice cores. <i>Nature</i> <b>366</b> , 552-554 (1993).	
241	29	Rhodes, R. H. et al. Enhanced tropical methane production in response to iceberg discharge in	
242		the North Atlantic. <i>Science</i> <b>348</b> , 1016-1019, doi:10.1126/science.1262005 (2015).	
243	30	Dee, D. P. et al. The ERA-Interim reanalysis: configuration and performance of the data	
244		assimilation system. Quarterly Journal of the Royal Meteorological Society <b>137</b> , 553-597,	
245		doi:10.1002/qj.828 (2011).	
		doi.10.1002/qj.828 (2011).	
246			
247	Acknowledgements. This work is funded through the U.S. National Science Foundation, grants		
248	ANT-1643394 (to C.B. and J.J.W.), ANT-1643355 (to T.J.F. and E.J.S), AGS-1502990 (to F.H.); the		
249	Swiss National Science Foundation grant 200021 143436 (to H.S.); CNRS/INSU/LEFE projects		
250	lcoCh	rono and CO2Role (to F.P.); JSPS KAKENHI grants 15H01731 (to K.GA., H.M. and M.H.),	
230	iceen		
251	15KK(	0027 (to K.K.) and 26241011 (to K.K., S.F. and H.M.); MEXT KAKENHI grant 17H06320 (to	
252	К.К.,	H.M. and R.U.); European Research Council under the European Community's Seventh	
	,		
252	Frame	work Programma (EP7/2007 2012)/EPC grant agreement (100EE (to LDD)), and the	
253	Frame	ework Programme (FP7/2007–2013)/ERC grant agreement 610055 (to J.B.P.) ; and the	
254	NOAA Climate and Global Change Postdoctoral Fellowship program, administered by the		
255	Univo	rsity Corporation for Atmospheric Research (F.H.). We acknowledge high-performance	
235	011100	and enperation for Acheophene Research (Fing. we device men performance	
256		the support from Velloutone (edu/05065/dz do ba) are thed to NOAD	
256	comp	uting support from Yellowstone (ark:/85065/d7wd3xhc) provided by NCAR's	

Computational and Information Systems Laboratory, sponsored by the NSF. This research used
 resources of the Oak Ridge Leadership Computing Facility at the Oak Ridge National Laboratory,
 which is supported by the Office of Science of the U.S. Department of Energy under Contract №
 DE-AC05-00OR22725. This is TALDICE publication № 52.

Author Contributions. Data analysis by C.B., M.Se., M.Si. and J.J.W.; manuscript preparation by C.B.; volcanic ice core synchronization by M.Si, M.Se., C.B., J.R.M., F.P., S.F. and T.J.F.; GCM simulations and interpretation by F.H., J.B.P. and J.J.W.; Moisture tagging/tracing experiments by B.R.M. and H.S.; Ice core water isotope analysis by K.G-A, K.K., H.M., M.H., R.U., B.S. and E.J.S.; all authors discussed the results and contributed towards improving the final manuscript.

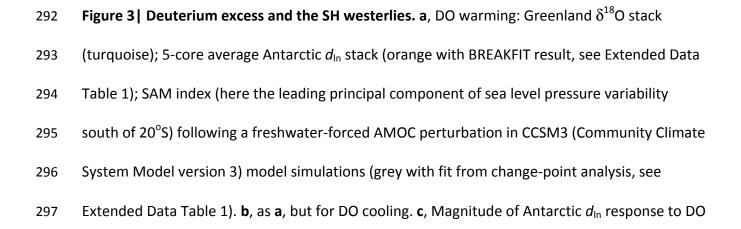
Author Information. permissions available 266 Reprints and information is at www.nature.com/reprints. The authors declare no competing financial interests. 267 Correspondence and requests for materials should be addressed to Christo Buizert (buizertc@ 268 oregonstate.edu). 269

Figure 1 | Records of abrupt glacial climate variability. a, Greenland Summit (average of GISP2 and GRIP<sup>28</sup>) ice core  $\delta^{18}$ O. b, WDC methane<sup>29</sup>. c, Antarctic 5-core average  $d_{ln}$  anomaly. d, Antarctic  $\delta^{18}$ O anomaly at EDML (blue), the Antarctic Plateau (average of DF and EDC, red) and 5-core average (black); offset for clarity. All records are synchronized to the WAIS Divide WD2014 chronology; Antarctic data are shown as anomalies relative to present. DO interstadial periods marked in grey and numbered; Heinrich stadials marked in blue. Isotope ratios are on the VSMOW (Vienna Standard Mean Ocean Water) scale. Thin curves show records at original 277 resolution (ranging from ~5 to ~50 years), with the thick lines a moving average (300 and 150
278 year window for Antarctic and Greenland data, respectively).

279

**Figure 2** | The Antarctic climate response to DO warming. a, Stack of NGRIP  $\delta^{18}$ O. b, Stack of 280 Antarctic  $\delta^{18}$ O at indicated locations, with "Plateau" the average of DF and EDC. **c**, As in **b**, but 281 with 5-core mean subtracted. **d**. First two principal components of the Antarctic  $\delta^{18}$ O stacks 282 283 (1500 yr window), with percentage of variance explained (offset for clarity). PC1 is strongly correlated (r = 0.998) to the Antarctic mean. Linear fit to PC1 (t = -400 to t=0 interval) is shown 284 to highlight the response around t = 0. **e**, Rotated PC1 and PC2 vectors representing proposed 285 286 oceanic and atmospheric modes, with fits from change point analysis (Methods). The oceanic mode lags by 211 ± 42 years; the atmospheric mode by 28 ± 40 years (1 $\sigma$  bounds; Extended 287 Data Table 1). f-g, Empirical Orthogonal Functions EOF1 and EOF2 associated with PC1 and PC2 288 289 in **d**, scaled to show the magnitude in permil. **h**, Spatial pattern associated with the atmospheric 290 mode as shown in **e**, scaled to permil. Isotope ratios are on the VSMOW scale.

291



warming in permil. The weak  $d_{ln}$  trend before and after the abrupt jump likely reflects the SST of SH vapor source waters following the thermal bipolar seesaw<sup>8,11</sup>. **d**, as **c**, but for DO cooling. Isotope ratios are on the VSMOW scale.

301

## Figure 4 | Attribution of the atmospheric mode of Antarctic temperature variability. a, 302 Comparison of PC2 of the 5 Antarctic $\delta^{18}$ O stacks as in Fig. 2d (pink, left axis) and the Antarctic 303 mean $d_{ln}$ stack as in Fig. 3a (black, right axis). Isotope ratios are on the VSMOW scale. **b**, 304 Correlation between a standardized monthly SAM index and SAT (2-meter temperature) in ERA-305 Interim<sup>30</sup> for 1979-2017 (shading, scale bar on right) with superimposed 850 hPa geopotential 306 307 height regressions (10 m contours) and the ice core atmospheric temperature mode from Fig. 2h (circles, scale bar from Fig. 2). Note that regions of anti-correlation are colored red (i.e. 308 warming in response to negative SAM shift). c, as panel b, but for a standardized PSA index. The 309 SAM and PSA are here taken to be PC1 and PC2 of the 850 hPa geopotential height field south 310 311 of 20°S, respectively. d, as panel b, but for a synthetic index of the atmospheric mode created 312 by regressing ERA-Interim SAT anomalies at the ice core sites onto the coefficients in Fig. 2h 313 (Methods).

314

# 315 Methods

Volcanic ice core synchronization: Volcanic reference horizons provide the most precise way to 316 synchronize ice-core age scales<sup>31-35</sup>. Within the last decade, progress has been made in 317 volcanically linking the EPICA (European Project for Ice Coring in Antarctica) Dome C (EDC) ice 318 core to the EPICA Dronning Maud Land (EDML) core<sup>31</sup>, the Talos Dome (TAL) core<sup>32</sup>, and the 319 Dome Fuji (DF) core<sup>33</sup>. Here we provide new volcanic stratigraphic links between the WAIS 320 (West Antarctic Ice Sheet) Divide ice core (WDC) and the EDML, EDC and TAL cores, based on 321 322 pattern matching of volcanic peaks in high-resolution records of either sulfur (WDC) or sulfate (EDML, EDC, TAL). Extended Data Fig. 1b summarizes the various synchronizations, with 323 previously published ones indicated with grey arrows, and the new ones presented here 324 indicated with colored arrows. 325

326 Volcanic synchronization via sulfur/sulfate and/or ECM (electrical conductivity measurements) records is a commonly-used technique for Antarctic ice cores, and we rely on previously 327 established methods described in detail elsewhere<sup>31-35</sup>. Matches are made by identifying 328 sequences of sulfur peaks that have the same relative spacing in both cores<sup>31-33,35</sup>. Additional 329 confidence in the match points comes from approximately proportional acid concentration 330 331 levels, smooth variations in the resulting annual layer thickness between stratigraphic tiepoints, and in some cases a distinctive shape of the common signals in the different ice cores. 332 We identify 773 volcanic ties between WDC and EDML, 396 between WDC and EDC, and 425 333 between WDC and TAL (Source Data). 334

335 Stratigraphic matching was performed independently by two authors (M.Si. and M.Se.), and 336 then compiled and compared by a third author (C.B.). Both analysts use an iterative approach, 337 in which they first identify the major, unambiguous events. After marking these events (or 338 clusters thereof), they re-align the data sets, and replot them with the marked events now 339 overlapping. At this point, usually several of the smaller events are nearly on top of each other. 340 These events are then marked, and the data is replotted with the newly marked events 341 overlapping, et cetera.

We distinguish three cases: "doubly", "singly", and "inconsistently" identified events. Doubly 342 identified matches are cases where both workers identify the same stratigraphic match 343 between two cores for a given volcanic event (within a margin of a few cm). Singly identified 344 matches are cases where only one of the two workers identified a stratigraphic match. 345 Inconsistently identified matches are cases where a single volcanic event in one core is linked to 346 two different volcanic events in the other core. Around 99% of the singly identified events were 347 found by M.Si., demonstrating a difference in event detection threshold. For example, in the 348 WDC-EDC synchronization the median volcanic peak sizes in WDC non-sea salt Sulfur (nssS) 349 were 67.7 and 31.4 ppb for the doubly and singly identified matches, respectively, 350 demonstrating that analyst M.Se. is more conservative in assigning match points. For 351 comparison, the background nssS level is 15±4 ppb. 352

Here, all the doubly identified events are all assumed correct, and retained. In the (relatively 353 rare) case of an inconsistently matched event, the stratigraphic links suggested by both workers 354 355 are discarded to avoid ambiguity. Sequences of singly identified events are retained only if they occur in between two doubly identified match points. In the case of an inconsistently identified 356 357 event (which is discarded), all singly identified matches adjacent to it are discarded also, until 358 another doubly identified match is encountered. In all three synchronizations, the vast bulk of the singly identified matches come from the same worker, suggesting a difference in style and 359 event detection threshold between the two workers. We give some examples below of 360 361 hypothetical sequences of tie points, and how they are dealt with. Let "d", "s" and "i" denote doubly, singly, and inconsistently identified tie points, respectively. 362

**d-s-s-s-d**: This is a hypothetical series of three **s** tie points in between two **d** tie points. Because both workers agree on the tie points on either end, there is no reason to assume the **s** tie points are incorrect; it simply reflects the fact that one worker (M.Se) is much more conservative in assigning tie points than the other worker (M.Si). Therefore all tie points are retained in the final synchronization (**d-s-s-s-d**). Singly identified ties are retained in such cases irrespective of how many are in the series (for example a series of 10 **s** ties would be retained if bracketed on either side by a **d**).

d-i-d: In this case the i tie is removed, but the d ties are retained resulting in the sequence d-din the final synchronization.

**d-s-s-i-s-d**: The **i** tie is removed in all cases. However, in this example the **s** tie points occur adjacent to an **i** tie point, which casts doubt on their reliability. Therefore they are removed together with the inconsistent tie, and only the sequence **d-d** is retained in the final synchronization.

The matching is described below for the 10-61ka interval of interest (the WDC-EDC synchronization extends back only to 57 ka BP).

In synchronizing WDC and EDC, the two workers identified 473 matches, out of which 103 were doubly, 8 inconsistently, and 362 singly identified (all but two of which by M.Si.). The final selection has retained the 103 doubly identified matches, and 293 of the singly identified matches; 69 singly identified matches were discarded as they were bracketed on either side by an inconsistent match. The 8 inconsistently identified matches all differed by less than 70 cm in EDC (or about 65 years).

In synchronizing WDC and EDML, the two workers identified a total of 793 matches, out of which 247 were doubly identified, 3 matches were inconsistently identified (all adjacent, and not separated by doubly identified events), and 543 were singly identified (all by M.Si.). The final selection has retained the 247 doubly identified matches, and 526 of the singly identified matches; 17 singly identified matches were discarded as they were bracketed on either side by an inconsistent match. The 3 inconsistently identified matches all differed by less than 1.6 m in EDML (or about 65 years).

Talos Dome proved to be the most difficult of the cores to synchronize, presumably because 391 the layers are more strongly compressed in this intermediate depth core. The first attempt at 392 synchronization yielded 55 doubly and 5 inconsistently identified matches, with most of the 393 errors in the 770 to 905 m depth range (up to 5 m offsets in TAL). In light of this inconsistency, 394 395 the workers reviewed their volcanic ties throughout the core, with particular focus on the 396 problematic interval. In the revised synchronization, the workers identified a total of 437 397 matches, out of which 253 were doubly identified, 4 matches were inconsistently identified (all adjacent, and not separated by doubly identified events), and 180 were singly identified (all but 398 399 9 by M.Si). The final selection has retained the 253 doubly identified matches, and 172 of the singly identified matches; 8 singly identified matches were discarded. The 4 inconsistently 400 401 identified matches all differed by less than 75 cm in TAL (or about 75 years). So while the final synchronization shows good agreement between both workers, we feel obliged to also report 402 403 the first, less successful attempt. The TAL depth range that is hardest to synchronize to WDC 404 (between 770 and 905 m TAL depth, or 14.9 to 25.2 ka BP) also yielded no matches to EDC in a published study<sup>32</sup> (see yellow triangles at bottom of Extended Data Fig. 1a). Note that this 405 problematic 15-25 ka time interval does not influence the main results of this work - none of 406 the abrupt DO events used in the stacking lie in this interval (DO 2 is excluded from the stacking 407 because the absence of an abrupt CH4 signal precludes precise synchronization to Greenland<sup>15</sup>). 408

The number of doubly and inconsistently identified events provides one way to assess the 409 reliability of the volcanic synchronization; the percentage of inconsistently identified events 410 (out of the pool of doubly and inconsistently identified events) ranges from 1% to 7% for the 411 three cores. Errors tend to occur in clusters of adjacent picks, due to the misidentification of a 412 413 sequence of peaks; seen in this light the WDC-EDML and WDC-TAL synchronizations each only contain a single inconsistently identified sequence. The observed inconsistencies were always 414 relatively small, and on the order of a few decades. A second method of assessing the reliability 415 is via the redundancy offered by having multiple cores. Whenever three ice cores in Extended 416 417 Data Fig. 1b are connected via three independent synchronizations (i.e., whenever the arrows form a triangle), this offers the possibility to test the internal consistency of the 418 synchronization. Over the age interval of interest (the last 61 ka) 213 ties had previously been 419 identified between EDML and EDC<sup>36</sup>, as well as 102 ties between TAL and EDC. This introduces a 420 degree of redundancy that allows testing the internal consistency of the synchronization. EDC, 421 422 TAL and EDML are volcanically synchronized within the AICC2012 (Antarctic Ice Core Chronology)<sup>36</sup>, while WDC uses the independent WD2014 time scale<sup>37,38</sup>. For each volcanic tie 423 point, the difference in WD2014 age minus the AICC2012 age is shown in Extended Data Fig. 1a. 424 EDC and EDML are volcanically synchronized over the last 60ka (blue triangles), and therefore 425 426 the excellent agreement between the blue (WDC age minus EDML age) and red (WDC age 427 minus EDC age) curves in Extended Data Fig. 1a shows the volcanic framework to be internally 428 consistent. Likewise, for the period 25-42 ka BP and <13 ka BP, where TAL and EDC are 429 volcanically synchronized (yellow triangles), the yellow (WDC age minus TAL age) and red (WDC 430 age minus EDC age) curves agree well, suggesting internal consistency. Beyond 42 ka BP the

431 yellow curve deviates from the blue and red ones, suggesting the TAL core is imperfectly432 synchronized within the AICC2012 chronology (due to an absence of volcanic ties at the time).

All ice cores used in this study were synchronized to the WAIS Divide WD2014 chronology<sup>37,38</sup>. 433 434 For the four non-WDC cores, we start from their original ice core chronologies; this is the AICC2012 chronology<sup>36</sup> for the EDML, EDC and TAL ice cores, and the DF2006 chronology for 435 the DF core<sup>39</sup>. For each core we add a time-variable offset to the WD2014 chronology that is 436 obtained using linear interpolation between the volcanic tie points. For the EDML, EDC and TAL 437 cores we have direct synchronizations to WDC as described above. For the Dome Fuji core, 438 439 synchronization was indirect via the EDC core (Extended Data Fig. 1b). Previously, 297 tie points have been identified<sup>33</sup> between EDC and DF in the interval of interest (mean spacing of 173) 440 years). These volcanic ties are transferred to WDC using the WDC-EDC synchronization 441 described above. 442

443 Over the time interval of interest, the offset with the AICC2012 cores (EDML, EDC, TAL) ranges 444 roughly from -330 years to + 430 years, with an average offset of -10 years (with negative 445 values meaning WD2014 is younger than AICC2012). For the DF core the range is from -230 to 446 1884 years, with an average of +739 years.

447 Uncertainty in volcanic synchronization: There are two types of uncertainty to consider. First, the volcanic ties themselves may be incorrect, and second, in between the ties the 448 interpolation strategy introduces an error. The first type is difficult to quantify. Either the ties 449 have been correctly identified, and the relative age uncertainty is zero, or the ties are false, and 450 451 the relative age uncertainty is infinite (i.e., we have learned nothing). Past studies have sometimes assigned Gaussian errors to volcanic tie points; while this is a practical necessity for 452 applications that optimize the fit to multiple age constraints<sup>36,40-42</sup>, it does not reflect the true 453 uncertainty meaningfully and is not applied here. 454

We have high confidence in the correctness of the volcanic ties because of the internal consistency of the new volcanic ties with previously published ones (Extended Data Fig. 1a), and the fact that doubly identified ties greatly outnumber the inconsistently identified ones. We have removed inconsistent matches from the synchronization, and we here assume the remaining matches to be correct.

The second type of uncertainty is due to interpolation between volcanic ties. This introduces an 460 age uncertainty that depends on the age difference between adjacent ties, L. We estimate the 461 interpolation uncertainty using the layer-counted section of the WD2014 chronology, which 462 463 goes back to 31.2 ka BP. To estimate the interpolation uncertainty for two volcanic markers that are, say, L=100 years apart, we can randomly pick thousands of 100-year intervals from the 464 WAIS Divide WD2014 chronology. Within each of these, the age evolution deviates from the 465 assumed linear interpolation;  $1\sigma$  standard deviation of this age deviation is used as the 466 interpolation uncertainty. Typical results are shown in Extended Data Fig. 2a for several values 467 of L. We find that the maximum uncertainty scales as  $\propto L^2$ . Compared to East Antarctica, West 468

Antarctica receives a larger contribution of its snowfall from storm systems and synoptic activity, making accumulation rates more variable<sup>43,44</sup>; the estimates given here should thus be considered conservative when used in interior Antarctica. The volcanic interpolation uncertainty for the four cores is plotted in Extended Data Fig. 2b. For DF, synchronization to WDC is done via EDC as an intermediary core, and therefore the two synchronization errors are added in quadrature.

In our synchronization we use both the singly and doubly identified tie points, and treat them 475 equally. We acknowledge, however, that the doubly identified ties are more reliable. Therefore, 476 477 we have repeated the analyses described in the main text using only the doubly identified tie 478 points (as opposed to both singly and doubly identified tie points). We find that the conclusions 479 of this work do not depend on this choice of tie points. Those tests are not shown here, but the alternative chronologies that use only the doubly identified tie points, and alternative versions 480 481 of the manuscript figures showing those analyses were presented to the reviewers and are available from the corresponding author upon request. 482

483 **Water stable isotope data:** A combination of previously published and unpublished ice core 484 water isotope data ( $\delta^{18}$ O and  $\delta$ D) are used in this study. Deuterium excess ( $d_{ln}$ ) is calculated 485 from the  $\delta^{18}$ O and  $\delta$ D isotope ratios using the logarithmic definition of Uemura et al.<sup>20</sup>:

486 
$$d_{\text{in}} = \ln(1+\delta D) - 8.47 \ln(1+\delta^{18}O) + 0.0285 [\ln(1+\delta^{18}O)]^2$$

487 For WDC we use previously published  $\delta^{18}$ O and  $\delta$ D data<sup>8,15,45</sup>, measured using laser 488 spectroscopy. Data have a typical depth resolution of 1m for the 0 to 2.3 ka BP interval, of 0.5 489 m for 2.3 to 56 ka BP, and of 0.25 m for 56-68 ka BP; this corresponds to an average time 490 resolution of 17 years for the study period (11 to 61 ka BP). Using the cm-scale CFA (continuous 491 flow analysis) record of WDC  $\delta^{18}$ O instead gives identical results to those presented here<sup>46</sup>.

- 492 For EDML we use previously published  $\delta^{18}$ O and  $\delta$ D data<sup>47,48</sup>, measured using conventional 493 IRMS (isotope ration mass spectrometry). Data have a typical depth resolution of 0.5 m, 494 corresponding to an average time resolution of 24 years for the study period.
- For EDC we use previously published  $\delta^{18}$ O and  $\delta$ D data<sup>48,49</sup>, measured using conventional IRMS. Data have a typical depth resolution of 0.55 m, corresponding to an average time resolution of 497 44 years for the study period.
- For DF we use new and published water isotope data<sup>39,50,51</sup>. Two data sets are used. The first is a data set of  $\delta^{18}$ O measured using IRMS in the 300 to 1151 m depth range (10 to 71 ka BP) at 0.5 m resolution<sup>50</sup>. The second is a data set of  $\delta^{18}$ O and  $\delta$ D measured using IRMS in the 550 to 849 m depth range (23 to 45 ka BP); this data set was measured at 0.1 m resolution, and averaged into 0.5 m bins. Note that  $d_{ln}$  is only available from the second data set, which spans DO/AIM (Antarctic Isotopic Maximum) evens 2 through 11. In the depth range of overlap,  $\delta^{18}$ O data from both data sets are averaged (after correcting the second data set by + 0.213‰ to

- account for a calibration offset) to produce the final time series. The combined  $\delta^{18}$ O record has an average time resolution of 35 years for the study period.
- For TAL we use a combination of new and previously published<sup>10,52,53</sup> data. Bag average, 1 m resolution  $\delta^{18}$ O and  $\delta$ D data measured using IRMS are available for the entire core. Highresolution (0.1 m)  $\delta^{18}$ O data measured using IRMS are available in the 598 to 786 m (10 to 16 ka BP) and 1030 to 1282 m (37 to 65 ka BP) depth ranges. High-resolution  $\delta^{18}$ O are averaged into
- 511 0.5 m bins, and combined with bag-average data for remaining depth intervals. The combined
- 512  $\delta^{18}$ O record has an average time resolution of 50 years for the study period.
- **Stacking procedure:** The stacking procedure used to investigate the Antarctic climate response to abrupt DO variability is described in detail elsewhere<sup>15</sup>. In short, the individual Greenland events are aligned at the midpoint of their abrupt  $\delta^{18}$ O transitions (either DO warming or DO cooling). All Antarctic events (on their volcanically-synchronized WD2014 timescales) are aligned at the midpoints of the abrupt WDC CH<sub>4</sub> transitions. We then average over events to obtain the shared climatic signal; to derive the north-south phasing we use the independently established CH<sub>4</sub> delay of 56 ± 19 years (1 $\sigma$ ) behind  $\delta^{18}$ O in Greenland<sup>54</sup>.
- For one of the abrupt events (DO-10 / AIM-10), improved inter-polar synchronization data are available from <sup>10</sup>Be variations during the Laschamp event (41 ka BP) between the Greenland NGRIP core, and the Antarctic EDC and EDML cores<sup>27</sup>; these timing constraints were incorporated into our stacking procedure (DO-10 only). The EDML, EDC, DF and TAL ice cores have much higher  $\Delta$ age uncertainty and lower resolution CH<sub>4</sub> records than WDC, therefore the north-south phasing precision cannot be improved by considering CH<sub>4</sub> synchronization for those cores also.
- In this work we consider DO-0 (i.e. the YD-Holocene transition) through DO-16; DO-17 falls outside the volcanic synchronization for the EDC and DF cores. DO-2 is omitted due to the absence of a clear  $CH_4$  response, precluding synchronization. All stacked records are shown in Extended Data Fig. 3.
- 531 Uncertainty in the timing of the stacked records comes from these sources: (1) The gas age-ice 532 age difference ( $\Delta$ age) in the WDC core<sup>37;</sup> (2) DO midpoint detection in the abrupt NGRIP  $\delta^{18}$ O 533 record; (3) DO midpoint detection in the abrupt WDC CH<sub>4</sub> record; (4) Interpolation of the WDC 534 chronology between tie points; (5) The climatic lag of atmospheric CH<sub>4</sub> behind Greenland  $\delta^{18}$ O 535 of 56 ± 19 years (1 $\sigma$ )<sup>54</sup>; (6) Trend analysis in the BREAKFIT<sup>55</sup> and RAMPFIT<sup>56</sup> fitting routines; and
- 536 (7) volcanic synchronization onto the WD2014 chronology.
- 537

538 The combined uncertainty due to the first 5 items was assessed previously using a Monte-Carlo 539 routine, suggesting a  $1\sigma$  timing uncertainty of 38 and 41 years in the WDC stacks for DO 540 warming and DO cooling, respectively<sup>15</sup>. The uncertainty in the trend analysis is given in 541 Extended Data Table 1. The uncertainty in the volcanic synchronization is shown in Extended Data Fig. 2; averaged over the stacked events the 1σ synchronization uncertainty is 0 years at
WDC, 2 years at EDML, 6 years at EDC, 13 years at DF, and 2 years at TAL.

544 By stacking only the most prominent DO/AIM events (those following Heinrich events; i.e., DO-545 4, 8, 12, 14 and 17) or just the minor ones (the remainder), we find that the magnitude of the 546 atmospherically-forced Antarctic response is larger for the former, suggesting proportionality 547 with the climate perturbation (Extended Data Fig. 4a-4f). Proportionality of the atmospheric 548 response is further seen for individual events (Extended Data Fig. 4g); see the figure caption for 549 details.

Principal Component Analysis: Principal component analysis (PCA) allows different climatic 550 modes to be identified in (paleoclimatic) time series from different locations<sup>57</sup>. Here we 551 perform PCA on the stacked  $\delta^{18}$ O records at the 5 individual sites using the MATLAB function 552 "pca". The  $\delta^{18}$ O stacks in the main manuscript combine 17 individual events – all those that fall 553 within the volcanic synchronization interval. To get a sense for the sensitivity to including or 554 555 excluding individual events, we perform additional experiments in which we stack only *n* events 556 (rather than all 17). The *n* events are randomly sampled without replacement (i.e. any given 557 event cannot be picked twice for each stacking). We then perform PCA of these stacked records (the same events are stacked for each of the cores), and standardize the PC vectors by taking 558 559 the z-score (or standard score). Extended Data Fig. 5 shows typical results for n=2 and n=8, 560 where for each n we repeat the experiment 50,000 times to obtain reliable statistics. Extended 561 Data Figs. 5a and 5b show PC1 and PC2, respectively, with the solid line showing the mean of 50,000 experiments, and the shaded envelope the associated +/-  $1\sigma$  standard deviation. 562 Extended Data Fig. 5c shows a histogram of the percentage of variance explained by each of the 563 564 modes.

We find that even by stacking as few as just *n*=2 events the method can, on average, identify the oceanic and atmospheric components described in the main manuscript. Perhaps not surprisingly, we find that when including fewer events the signal-to-noise ratio decreases: with fewer events the estimated signal amplitude is smaller in both PC1 and PC2, and the uncertainty envelope is wider. As more events are included in the stacking, the percentage of variance explained by PC1 increases as the coherence between the various Antarctic cores increases due to an improved signal-to-noise ratio.

Analysis in the main manuscript uses a 1500-year window (centered around t = 100 yr), which is 572 573 chosen because it corresponds to the recurrence time of the shortest DO cycles<sup>58-61</sup>. The 574 variance explained by the oceanic and atmospheric modes depends on the window length, as shown in Extended Data Fig. 6a. For window lengths exceeding ~750 years, the "oceanic" mode 575 explains most of the variance (PC1), with the "atmospheric" mode explaining less. However, at 576 577 short window lengths (<750 year) the atmospheric mode explains most of the variance, making it PC1. Comparing PC1 at 400-year window to PC2 at 2000-year window (Extended Data Fig. 6b) 578 579 illustrates the ability of the PCA to identify the atmospheric mode at different window lengths.

The cross-over behavior (i.e. the atmospheric mode shifts from being PC2 to PC1 as a function of window length) is due to the fact that the signal variance of the step-like atmospheric mode occurs chiefly within the t = 0 to t = 100 interval; signal variance of the oceanic mode depends strongly on the window length, due to its gradual nature.

Lag time analysis of PC1 and PC2 using the RAMPFIT<sup>56</sup> and BREAKFIT<sup>55</sup> routines confirms the cross-over behavior. At short window-length (<700 years), PC1 is characterized by the instantaneous /fast response of the hypothesized atmospheric teleconnection, whereas at large window-length (>800 years) it shows the 200-year delayed hypothesized oceanic teleconnection. PC2 shows the opposite behavior, though note that for PC2 at 400-year window length no meaningful solution can be found with either routine. At window lengths >700 years the lag times remain stable and vary only within the uncertainty bound.

591 Unless specified otherwise, a 1500-year window is used in this work.

## 592 **Robustness of the atmospheric spatial pattern:**

The spatial pattern we identify for the atmospheric mode is one of the main results of this work, and we here test its robustness. In Extended Data Figs. 6d—6f we compare three alternative ways of identifying the spatial pattern; the Pearson correlation coefficient (r) between the shown pattern and the pattern identified in the main text (EOF 2 at 1500 yr window) is given for each. Details on the three methods are given in the figure caption. Correlation coefficients ranging from r = 0.92 to r = 0.999 suggest that identification of the atmospheric pattern is both qualitatively and quantitatively robust.

Rotated PCA vectors: PCA aims to explain the largest amount of variance, whereas our goal is 600 to distinguish between the oceanic and atmospheric modes. While PC1 is clearly dominated by 601 the 200-year-delayed oceanic bipolar seesaw (Fig. 2d), it appears that PC1 also captures some 602 abrupt warming around t = 0, apparently due to the fact that atmospherically-induced warming 603 is more prevalent over Antarctica than cooling (NH DO warming case). We therefore construct 604 (admittedly somewhat subjective) oceanic and atmospheric response functions (Fig. 2e), which 605 are derived from the principal components in the following way. Let PC1 and PC2 be the first 606 607 two principal components through time; these vectors are perpendicular. We let the 608 atmospheric response ATM be identical to PC2. The oceanic response OCE is found by rotating 609 the PC1 vector in the plane spanned by vectors PC1 and PC2 over an angle of -13 degrees:

610 OCE = 
$$\cos(-13^\circ) \times PC1 + \sin(-13^\circ) \times PC2$$

The rotation angle of -13 degrees is picked such that the  $\delta^{18}$ O shift at t = 0 is minimized. The

spatial pattern associated with the ATM response (Fig. 2h) is found by multiple linear regression

of the  $\delta^{18}$ O stacks at the individual sites to OCE and ATM using the MATLAB function "regress".

614 **SAM, PSA and synthetic "atmospheric" indices.** The SAM and PSA indices were calculated from 615 climate model and reanalysis data as respectively the first and second mode of variability in

PCA/EOF analysis (MATLAB function "pca") of sea-level pressure (model) or 850-hPa 616 geopotential height (reanalysis) south of 20°S, after subtracting the long term mean and scaling 617 the anomalies by the square root of the cosine of latitude to account for the decreased surface 618 area closer to the poles. A synthetic index of the inferred atmospheric teleconnection is created 619 620 by projecting reanalysis SAT anomalies at the ice core locations onto the atmospheric loading 621 coefficients from Fig. 2h, the spatial signature of which is shown in Fig. 4d. Mathematically, this 622 projection is done by multiplying the SAT anomalies with the loading coefficients, and summing 623 over them at each monthly time step.

It is worth noting that all these inferences with respect to reanalysis data are reliant upon just five atmospheric loading coefficients from the limited (from the perspective of the large-scale circulation) spatial domain of Antarctica, so it is difficult to rigorously exclude non-SAM atmospheric influences from the temperature pattern alone.

628 In Extended Data Fig. 9 we compare variability in the SH westerly winds in the glacial CCSM3 (Community Climate System Model version 3) climate simulations<sup>25,62</sup> to the ERA-Interim 629 reanalysis<sup>30</sup>. Both show greater variability in the Indian and Pacific sectors, relative to the 630 Atlantic sector. Compared to ERA-interim, the CCSM3 SAM is more zonal/annular in its 631 632 structure; the CCSM3 westerlies also appear to have smaller variability (some of this difference could be due to comparing annual mean with decadal mean data). In CCSM3 the forced 633 response of the SH westerlies (at 19ka in response to increased North Atlantic freshwater, right 634 panel) is very similar to the internal variability of the SH westerlies (middle panel), suggesting 635 that the change in the SH atmospheric circulation induced by freshwater forcing in the North 636 637 Atlantic is analogous to the existing mode of internal variability.

To estimate the magnitude of SAM shifts of the DO cycle, we analyze the changes in central 638 639 East Antarctica where the signal is largest and most consistent with the present-day observed relationship (Fig. 4). Using an isotope sensitivity of 0.8 % K<sup>-1</sup>, the atmospherically-induced 640 temperature anomaly in central East Antarctica (DF, EDC) is in the range of 0.20°C to 0.45°C 641 642 during a DO-warming (lower and upper bound reflecting typical minor and major DO/AIM events, respectively). Regression of ERA-interim 2m temperature at DF and EDC to the SAM 643 index shows a slope of around -1.2°C per unit of normalized SAM (the normalized SAM index 644 time series has a standard deviation of 1), implying a shift in SAM index of around 0.2 to 0.4 645 646 normalized (modern-day) SAM units (rounded to one significant figure). This estimate assumes (1) a linear isotope-temperature response using the modern-day spatial slope, and (2) that the 647 648 monthly SAM-SAT regression from monthly internal SAM variability also applies to persistent SAM shifts during the glacial; both assumptions are subject to uncertainties that we do not 649 650 address here. The CCSM3 model simulates a persisting SAM shift of the same magnitude as the internal SAM variability in decadal averaged data (Fig.3); because internal SAM variability will 651 652 be larger in monthly than in decadally-averaged data, the model and data-based estimates may 653 be in agreement. The reanalysis time period is too short to derive robust estimates of decadally 654 averaged SAM variability.

655 **GCM simulations**. We used the TraCE-21k transient climate model simulations done with the 656 Community Climate System Model version 3 (CCSM3)<sup>25,62-65</sup>. AMOC collapse and resumption are 657 triggered using freshwater forcing in the North Atlantic. The "DGL19k" run is used for the 658 AMOC collapse, the "DGL-overshoot-C" run for the AMOC resumption case<sup>64</sup>.

659 **Moisture origin analysis**. We use two separate experiments that trace moisture origin of the 660 precipitation at the coring sites.

The first method uses a Lagrangian moisture source diagnostic<sup>66</sup> based on a previously 661 published data set<sup>67</sup>. Using the winds, temperature and humidity of the ERA-Interim reanalysis 662 data set<sup>30</sup> covering the years 1980-2013, 5 million air parcel trajectories have been calculated 663 covering the global atmosphere at 6-hourly resolution using the Lagrangian particle dispersion 664 model FLEXPART<sup>68</sup>. From the analysis of specific humidity changes over time along the air 665 parcel trajectories, moisture sources have been identified whenever specific humidity in the air 666 parcels increased more than a threshold value of 0.1 g kg<sup>-1</sup> over a 6-hour period. The fractional 667 contribution of each moisture source to the final precipitation at the target location (an area of 668 300×300 km centered on each ice core site) is obtained from calculating the amount 669 contributed by a moisture source to the humidity already present in an air parcel. During 670 precipitation en route, the previous sources' contributions are proportionally discounted. This 671 results in a quantitative estimate of the contribution of surface areas to the precipitation in the 672 target region in units of evaporation (water mass per unit area per time), including their 673 position in terms of latitude and longitude. The moisture source contributions for each site and 674 precipitation event have been composited into mass-weighted annual mean values and scaled 675 676 with respect to the total amount of water deposited at the target region.

The second method uses water tagging in a 50-year simulation with the Community 677 678 Atmosphere Model (CAM), with prescribed seasonally varying SST and modern boundary conditions. The experiment is set up to evaluate the meridional moisture source distribution, 679 with further details and figures given in Ref.<sup>8</sup>. In short, evaporation is tagged in 11 bins. One bin 680 is the Antarctic continent (re-evaporation) and ocean and ice shelfs south of 70°S; 10 are zonal 681 bins of 5° latitude each, ranging from 20°S to 70°S. For each core, the moisture source 682 distribution is found by evaluating the relative contributions from each of the bins for the last 683 30 years of the run. Two moisture source distributions were created, one for all year in which 684 685 the mean annual SAM index was positive, and one for all years in which it was negative (Extended Data 8b). 686

**Change point detection**. We use two well-documented and widely-used change-point detection methods: BREAKFIT<sup>55</sup> and RAMPFIT<sup>56</sup>, with results given in Extended Data Table 1. The choice of which one to use is based on the shape of the time series x(t). BREAKFIT finds a single changepoint, and fits a linear slope on either side; these features make it suitable for the oceanic mode / PC1 in the main manuscript. RAMPFIT finds two change-points; it is assumed x(t) has constant value  $x_1$  for  $t < t_1$ , then a ramp up or down until it reaches value  $x_2$  at time  $t_2$ , after which it remains constant at value  $x_2$  for  $t > t_2$ . These features make RAMPFIT suitable for the atmospheric mode / PC2 in the main manuscript. To find the two change-points in the  $d_{ln}$ stacks, we applied both the RAMPFIT algorithm, and the BREAKFIT algorithm twice (once for each change-point). The results are comparable (Extended Data Table 1), and in the main text we report the average of both methods.

698

## 699 Methods References:

- Severi, M. *et al.* Synchronisation of the EDML and EDC ice cores for the last 52 kyr by volcanic
  signature matching. *Clim. Past* **3**, 367-374, doi:10.5194/cp-3-367-2007 (2007).
  Severi, M., Udisti, R., Becagli, S., Stenni, B. & Traversi, R. Volcanic synchronisation of the EPICA-
- 702
   32
   Severi, M., Odisti, R., Becagli, S., Stenni, B. & Traversi, R. Volcanic synchronisation of the EPICA 

   703
   DC and TALDICE ice cores for the last 42 kyr BP. *Clim. Past* **8**, 509-517, doi:10.5194/cp-8-509 

   704
   2012 (2012).
- Fujita, S., Parrenin, F., Severi, M., Motoyama, H. & Wolff, E. W. Volcanic synchronization of
  Dome Fuji and Dome C Antarctic deep ice cores over the past 216 kyr. *Clim. Past* 11, 1395-1416,
  doi:10.5194/cp-11-1395-2015 (2015).
- Sigl, M. *et al.* Insights from Antarctica on volcanic forcing during the Common Era. *Nature Clim. Change* 4, 693-697, doi:10.1038/nclimate2293 (2014).
- 710 35 Parrenin, F. *et al.* Volcanic synchronisation between the EPICA Dome C and Vostok ice cores
  711 (Antarctica) 0–145 kyr BP. *Clim. Past.* 8, 1031-1045 (2012).
- Veres, D. *et al.* The Antarctic ice core chronology (AICC2012): an optimized multi-parameter and
  multi-site dating approach for the last 120 thousand years. *Clim. Past* 9, 1733-1748,
  doi:10.5194/cp-9-1733-2013 (2013).
- 71537Buizert, C. *et al.* The WAIS Divide deep ice core WD2014 chronology part 1: Methane716synchronization (68-31 ka BP) and the gas age-ice age difference. *Clim. Past.* **11**, 153-173,717doi:10.5194/cp-11-153-2015 (2015).
- 718
   38
   Sigl, M. *et al.* The WAIS Divide deep ice core WD2014 chronology Part 2: Annual-layer counting

   719
   (0–31 ka BP). *Clim. Past* **12**, 769-786, doi:10.5194/cp-12-769-2016 (2016).
- 72039Kawamura, K. *et al.* Northern Hemisphere forcing of climatic cycles in Antarctica over the past721360,000 years. *Nature* **448**, 912-916, doi:10.1038/nature06015 (2007).
- 40 Bazin, L. *et al.* An optimized multi-proxy, multi-site Antarctic ice and gas orbital chronology
  (AICC2012): 120–800 ka. *Clim. Past* 9, 1715-1731, doi:10.5194/cp-9-1715-2013 (2013).
- Parrenin, F. *et al.* IceChrono1: a probabilistic model to compute a common and optimal
  chronology for several ice cores. *Geosci. Model Dev.* 8, 1473-1492, doi:10.5194/gmd-8-14732015 (2015).
- 42 Lemieux-Dudon, B. *et al.* Consistent dating for Antarctic and Greenland ice cores. *Quat. Sci. Rev.*728 29, 8-20, doi:10.1016/j.quascirev.2009.11.010 (2010).
- Fudge, T. J. *et al.* Variable relationship between accumulation and temperature in West
  Antarctica for the past 31,000 years. *Geophys. Res. Lett.* 43, 2016GL068356,
  doi:10.1002/2016gl068356 (2016).
- Fortuin, J. & Oerlemans, J. Parameterization of the annual surface temperature and mass
  balance of Antarctica. *Ann. Glaciol* 14, 78-84 (1990).
- 73445WAIS Divide Project Members. Onset of deglacial warming in West Antarctica driven by local735orbital forcing. Nature 500, 440-444, doi:10.1038/nature12376 (2013).
- Jones, T. R. *et al.* Water isotope diffusion in the WAIS Divide ice core during the Holocene and
  last glacial. *Journal of Geophysical Research: Earth Surface*, 2016JF003938,
  doi:10.1002/2016JF003938 (2017).

739	47	EPICA Community Members. One-to-one coupling of glacial climate variability in Greenland and
740		Antarctica. Nature <b>444</b> , 195-198, doi:10.1038/nature05301 (2006).
741	48	Stenni, B. et al. The deuterium excess records of EPICA Dome C and Dronning Maud Land ice
742		cores (East Antarctica). <i>Quat. Sci. Rev.</i> 29, 146-159, doi:10.1016/j.quascirev.2009.10.009 (2010).
743	49	Jouzel, J. et al. Orbital and millennial Antarctic climate variability over the past 800,000 years.
744		Science <b>317</b> , 793-796, doi:10.1126/science.1141038 (2007).
745	50	Kawamura, K. et al. State dependence of climatic instability over the past 720,000 years from
746		Antarctic ice cores and climate modeling. Science Advances 3, doi:10.1126/sciadv.1600446
747		(2017).
748	51	Uemura, R. et al. Asynchrony between Antarctic temperature and CO2 associated with obliquity
749		over the past 720,000 years. <i>Nature Communications</i> <b>9</b> , 961, doi:10.1038/s41467-018-03328-3
750		(2018).
751	52	Stenni, B. et al. Expression of the bipolar see-saw in Antarctic climate records during the last
752		deglaciation. <i>Nat. Geosci.</i> <b>4</b> , 46-49, doi:10.1038/ngeo1026 (2011).
753	53	Landais, A. et al. A review of the bipolar see-saw from synchronized and high resolution ice core
754		water stable isotope records from Greenland and East Antarctica. Quat. Sci. Rev. 114, 18-32,
755		doi:10.1016/j.quascirev.2015.01.031 (2015).
756	54	Baumgartner, M. et al. NGRIP CH4 concentration from 120 to 10 kyr before present and its
757		relation to a $\delta$ 15N temperature reconstruction from the same ice core. Clim. Past <b>10</b> , 903-920,
758		doi:10.5194/cp-10-903-2014 (2014).
759	55	Mudelsee, M. Break function regression. The European Physical Journal-Special Topics 174, 49-
760		63 (2009).
761	56	Mudelsee, M. Ramp function regression: a tool for quantifying climate transitions. Computers &
762		Geosciences <b>26</b> , 293-307 (2000).
763	57	Clark, P. U., Pisias, N. G., Stocker, T. F. & Weaver, A. J. The role of the thermohaline circulation in
764		abrupt climate change. <i>Nature</i> <b>415</b> , 863-869, doi:10.1038/415863a (2002).
765	58	Grootes, P. M. & Stuiver, M. Oxygen 18/16 variability in Greenland snow and ice with 10–3- to
766		105-year time resolution. J. Geophys. Res. 102, 26455-26470, doi:10.1029/97jc00880 (1997).
767	59	Alley, R. B., Anandakrishnan, S. & Jung, P. Stochastic resonance in the North Atlantic.
768		Paleoceanography <b>16</b> , 190-198, doi:10.1029/2000pa000518 (2001).
769	60	Buizert, C. & Schmittner, A. Southern Ocean control of glacial AMOC stability and Dansgaard-
770		Oeschger interstadial duration. Paleoceanography <b>30</b> , 2015PA002795,
771		doi:10.1002/2015pa002795 (2015).
772	61	Ditlevsen, P. D., Kristensen, M. S. & Andersen, K. K. The recurrence time of Dansgaard-Oeschger
773		events and limits on the possible periodic component. J. Clim. 18, 2594-2603,
774		doi:10.1175/jcli3437.1 (2005).
775	62	He, F. et al. Northern Hemisphere forcing of Southern Hemisphere climate during the last
776		deglaciation. Nature <b>494</b> , 81-85, doi:10.1038/nature11822 (2013).
777	63	Liu, Z. et al. Younger Dryas cooling and the Greenland climate response to CO2. Proc. Natl. Acad.
778		Sci. U. S. A. (2012).
779	64	He, F. Simulating Transient Climate Evolution of the Last deglaciation with CCSM3, University of
780		Wisconsin-Madison 2010, (2010).
781	65	Pedro, J. B. et al. The spatial extent and dynamics of the Antarctic Cold Reversal. Nature Geosci
782	_	<b>9</b> , 51-55, doi:10.1038/ngeo2580 (2016).
783	66	Sodemann, H., Schwierz, C. & Wernli, H. Interannual variability of Greenland winter precipitation
784		sources: Lagrangian moisture diagnostic and North Atlantic Oscillation influence. J. Geophys.
785		<i>Res</i> . <b>113</b> , D03107, doi:10.1029/2007JD008503 (2008).

786 67 Läderach, A. & Sodemann, H. A revised picture of the atmospheric moisture residence time.
787 *Geophys. Res. Lett.* 43, 924-933, doi:10.1002/2015GL067449 (2016).
788 68 Stohl, A., Forster, C., Frank, A., Seibert, P. & Wotawa, G. Technical note: The Lagrangian particle

- 789
   dispersion model FLEXPART version 6.2. Atmos. Chem. Phys. 5, 2461-2474, doi:10.5194/acp-5 

   790
   2461-2005 (2005).
- 791 69 Locarnini, R. A. *et al.* in *NOAA Atlas NESDIS* 73 (eds S. Levitus & A. MIshonov) (2013).
- 70 Kalnay, E. *et al.* The NCEP/NCAR 40-year reanalysis project. *Bulletin of the American* 793 *meteorological Society* **77**, 437-471 (1996).

794

795 Data Availability. Source Data (WDC sulfur data, volcanic tie points and water isotope data on 796 synchronized chronologies) and derived products (stacks, PCA results, etc.) are available with 797 the online version of the paper, and via the NOAA paleoclimate data archive.

798

799 **Code Availability**. MATLAB code used for the stacking procedure can be found in the 800 supplementary information of ref.<sup>15</sup>, and is available from the corresponding author upon 801 request.

802

803 Extended Data Figure 1 | Volcanic synchronization of Antarctic ice cores. a, Age offset between the WD2014<sup>37,38</sup> (WDC) and AICC2012<sup>36</sup> (TAL, EDML, EDC) age scales, with each dot 804 representing a volcanic tie point. Yellow and blue triangles denote the timing of TAL-EDC and 805 EMDL-EDC volcanic ties<sup>32,36</sup>, respectively. **b**, Overview of synchronizations between the ice 806 807 cores used in this study. Previously published synchronizations are in grey; synchronization presented here are in color. Synchronizations within Antarctica are based purely on volcanic 808 809 links; synchronization between WDC and NGRIP (Greenland) are based on atmospheric CH<sub>4</sub> (green arrow). 810

811

Extended Data Figure 2 | Age uncertainty due to volcanic synchronization. a, Interpolation uncertainty (1 $\sigma$ ) for 4 different values of *L* (the spacing between two adjacent volcanic tie points), based on the layer-counted WD2014 age scale<sup>38</sup>. b, Interpolation uncertainty in synchronizing the 4 ice cores to WAIS Divide. Grey vertical lines give the timing of DO events.

816

Extended Data Figure 3 | Site-specific stacks of  $\delta^{18}$ O and  $d_{ln}$ . a, Stack of NGRIP  $\delta^{18}$ O (teal, left axis) and WDC CH<sub>4</sub> (green, right axis) during DO warming. b, As in a, but for DO cooling. c, Stack of Antarctic  $\delta^{18}$ O at indicated locations (see color legend) during DO warming. d, As in c, but for B20 DO cooling. **e**, Stack of Antarctic  $d_{ln}$  at indicated locations (see color legend) during DO B21 warming. **f**, As in **e**, but for DO cooling. Isotope ratios are on the VSMOW scale.

822

823

Extended Data Figure 4 Proportionality of the atmospheric response. Panels a-f compare 824 825 stacks of just the major DO/AIM events (those following Heinrich events, namely DO/AIMO, DO/AIM1, DO/AIM4, DO/AIM8, DO/AIM12 and DO/AIM14, left panels), and just the minor 826 DO/AIM events (the remainder, right panels). **a,b**, stacks of NGRIP  $\delta^{18}$ O (left axis) and CH4 (right 827 axis). **c.d**. Stacks of Antarctic  $\delta^{18}$ O at indicated locations. **e,f**, Same as panels **c** and **d**, but with 828 Antarctic mean subtracted. g, Proportionality of the atmospheric response for individual events 829 (numbered). NGRIP event size is found via regression of individual NGRIP events to the multi-830 event NGRIP  $\delta^{18}$ O stack normalized to unit variance (Fig. 2a). The Antarctic atmospheric 831 response is found via multiple linear regression of single-site, individual events to the 832 833 atmospheric and oceanic modes (Fig. 2e). Shown are average (dots) and standard deviation 834 (grey error bars) of the response at EDC, DF and EDML (the cores with the strongest atmospheric response); the EDML response is multiplied by -1 as it has the opposite sign of the 835 response at DF and EDC. Red and blue dots denote the major and minor DO/AIM events, 836 respectively. Isotope ratios are on the VSMOW scale. 837

838

Extended Data Figure 5 | Reducing the number of events in the  $\delta^{18}$ O stacks. **a**, PC1 when stacking 2 or 8 randomly selected events; thick line and shaded area represent the mean and +/- 1 $\sigma$  standard deviation of 50,000 runs, respectively. Vertical yellow bars denote the 200-year period after the abrupt DO event at t = 0. **b**, as panel **a**, but for PC2. **c**, Histogram of percentage of signal variance explained by PC1 and PC2, when stacking 2 or 8 randomly selected events. Color coding as in panels **a** and **b**.

845

846 Extended Data Figure 6| Robustness of the atmospherically-forced warming pattern. a, 847 Principal Component analysis as function of window length, with percent variance explained by PC1 and PC2. b, Comparison of PC1 at 400 year window length, to PC2 at 2000 year window 848 length, to show the cross-over of the atmospheric response (i.e. from PC1 to PC2) as a function 849 of window length. c, Lag time of the Antarctic PC1 and PC2 response as a function of window 850 length, assessed using BREAKFIT<sup>55</sup> and RAMPFIT<sup>56</sup> routines (see Methods for explanation of 851 which one is used). d, EOF1 at 400 year window length scaled to permil units. e, EOF2 at 2000 852 year window length scaled to permil units. **f**, Slope of linear fit to  $\delta^{18}$ O stacks in the t = 0 to t = 853 +200 year interval, shown as the change in permil during the 200 years. Isotope ratios are on 854 855 the VSMOW scale.

856

- 857 Extended Data Figure 7 | The Antarctic climate response to DO cooling. a, Stack of NGRIP
- 858  $\delta^{18}$ O. **b**, Stack of Antarctic  $\delta^{18}$ O at indicated locations. **c**, As in **b**, but with Antarctic mean
- subtracted. **d**, First two principal components of the Antarctic  $\delta^{18}$ O stacks, with percentage of

- 860 variance explained (offset for clarity) Lines show the BREAKFIT (PC1) and RAMPFIT (PC2) fits. e-
- **f**, Empirical Orthogonal Functions EOF1 and EOF2 associated with PC1 and PC2 in **d**, scaled to
- show the magnitude in permil. Isotope ratios are on the VSMOW scale.
- 863

Extended Data Figure 8 | Moisture sources of Antarctic ice core and the SAM. a, Mass-864 weighted probability distribution functions (PDFs) of Antarctic moisture sources for the five ice 865 cores of interest  $(5 \times 10^{-5} \text{ deg}^{-2} \text{ contour lines})$ ; the area integrated PDF equals 1). Distributions are 866 calculated from reanalysis data<sup>30,67</sup> using a Lagrangian source diagnostic<sup>21,66</sup> (Methods). 867 Parallels are plotted in  $15^{\circ}$  increments of latitude; meridians in  $45^{\circ}$  increments of longitude. **b**, 868 Sea surface temperature (SST, black)<sup>69</sup> and relative humidity (RH, grey)<sup>70</sup> as a function of 869 latitude. The colored curves give the latitudinal source distribution during negative SAM phase 870 (solid curves, SAM index < 0) and positive SAM phase (dashed curves, SAM index > 0). The solid 871 and open dots show the first moment of the source distribution during negative and positive 872 SAM phase, respectively. Note that during a positive SAM phase moisture sources for all core 873 locations are located closer to the Antarctic continent. Source distribution data were obtained 874 using water tagging experiments<sup>8</sup> in the Community Atmosphere Model (Methods). 875

876

877 Extended Data Figure 9 | Southern Annular Mode-like variability in zonal near-surface winds. a, ERA-Interim reanalysis (1979-2016 annual means) zonal wind speed at 10 m height regressed 878 onto SAM index (here the first principal component of sea level pressure variability south of 879  $20^{\circ}$ S), expressed in units of m s<sup>-1</sup> per standard deviation in the index. **b**, Same as panel **a**, but for 880 internal variability in the CCSM3 SynTraCE model simulation<sup>25,62</sup> during glacial climate prior to 881 freshwater forcing of Heinrich stadial 1 (19.5ka to 19.01ka BP, decadal means). c, Same as panel 882 a, but for the response to North Atlantic freshwater forcing in the CCSM3 SynTraCE model 883 (19.1ka to 18.9ka BP, decadal means, with the freshwater forcing applied at 19ka). 884

885

Extended Data Table 1 | Change-point analysis on Antarctic response. Change-points are 886 found using the BREAKFIT<sup>55</sup> or RAMPFIT<sup>56</sup> routine as indicated; the parameter  $t_{OCE}$  is the single 887 change-point of the oceanic mode;  $t_{ATM1}$  and  $t_{ATM2}$  are the two change-points of the 888 atmospheric mode, representing the onset and ending of the shift, respectively (Methods). 889 Stated uncertainties give the  $1\sigma$  value in the fitting routine only, found using a Monte Carlo 890 moving block bootstrap analysis with 1000 iterations<sup>55,56</sup>; the full uncertainty in the combined 891 interpolar CH<sub>4</sub> synchronization and stacking procedure<sup>15</sup> is estimated to be around 40 years 892  $(1\sigma)$ , which can mostly be attributed to uncertainty in the WAIS Divide ice age-gas age 893 difference  $\Delta age^{37}.$  The  $\delta^{18}\text{O}$  PC2 and  $\delta^{18}\text{O}$  atmospheric modes are identical. 894

